ChemElectroChem

Research Article
doi.org/10.1002/celc.202400291

Chemistry Europe
European Chemical Societies Publishing

www.chemelectrochem.org

Metal Alloy-Functionalized 3D-Printed Electrodes for Nitrate-to-Ammonia Conversion in Zinc-Nitrate Batteries

Si Liu[+],[a] Yupeng Zhao[+],[a, b] Zhengfan Chen,[a, b] Dandan Gao,[a, b] Fan Feng,[a, b] Tobias Rios-Studer,[b] Joachim Bansmann,[c] Johannes Biskupek,[d] Ute Kaiser,[d] Rongji Liu,*[a, b] and Carsten Streb*[a, b]

Electrocatalytic nitrate reduction is a promising approach to remove harmful nitrate and produce ammonia in aqueous media. Here, we demonstrate how 3D printed polymer electrodes can be electroless plated with a bimetallic NiCu alloy film suitable for sustained nitrate-to-ammonia reduction. Characterization by powder X-ray diffraction, X-ray photoelectron spectroscopy, scanning/transmission electron microscopy and energy-dispersive X-ray spectroscopy indicate that the electrode has a two-layer structure consisting of polymer/ coating layer of metal alloys. The composite electrode shows high-performance in the nitrate-to-ammonia electroreduction, giving NH_3 Faradaic efficiencies of up to 83% and NH_3 yield rates up to 860 μg/(h cm^2) at −0.38 V vs. RHE. We show that the electrode can easily be integrated into a Zn-nitrate battery, giving a power density of 3.8 mW cm^{-2} with continuous NH_3 production. The system combines three productive outputs, that is removal of nitrate pollutants, synthesis of valuable ammonia and generation of "green" electricity.

Introduction

NH_3 is a fundamental indispensable ingredient for chemical synthesis, agriculture and pharmaceuticals industry.[1,2] Large scale production of NH_3 was not feasible until the Haber-Bosch process was developed, which requires high temperature and pressure to drive the combination reaction of N_2 and H_2.[3,4] This process has dramatically improved the production of fertilizer and facilitated the manufacture of nitrogen-containing compounds in industry. However, as a result of the high energy barrier of the reaction and the growing demand for NH_3, Haber-Bosch cost nearly 2% of global energy and result in 400 Mt of CO_2 emission yearly.[5–7] To address this problem, the reduction of N_2 to NH_3 (NRR) using H_2O as the proton source and powered by renewable electricity has garnered public attention due to its potential to address CO_2 emissions and offer a sustainable pathway for the future NH_3 industry. However, the high energy barrier for breaking the N≡N triple bond and the low-efficiency mass transport at the gas-liquid-solid interface significantly impede this approach. As an alternative, the nitrate (NO_3^-) electroreduction to NH_3 (NO_3RR) is energetically more favorable than direct NRR for NH_3 electrosynthesis, particularly since nitrate is an ubiquitous water pollutant (due to intensive agriculture), has a high water solubility and a low dissociation energy for the N=O bond. Thus, ammonia generation by nitrate reduction could be an efficient path to access a valuable chemical while removing aqueous pollutants.

The conversion of NO_3^- to NH_3 is a complex proton-coupled eight electron process involving a sequence of intermediates. According to theoretical studies, Cu binds hydrogen poorly but adsorbs nitrate radicals and NO_3RR intermediates strongly, resulting in remarkable selectivity for NH_3 generation.[8,9] In addition to metallic Cu, CuO, Cu_2O, and Cu_3P were also reported as NO_3RR catalysts with high Faradaic efficiency (FE).[10–15] Furthermore, bimetallic or multimetallic Cu alloys exhibit higher activity and selectivity than monometallic Cu-based electrocatalysts, allowing for controllable intermediate adsorption and increased conversion efficiency by adjusting the elemental composition and electronic structure of the catalyst.[16–22]

In addition to the activity and selectivity of the catalyst itself, the architecture, conductivity, and cost of the substrates must all be addressed in consideration of manufacturing the supporting electrodes. An ideal electrode substrate should facilitate mass transfer, possess a large specific surface area for catalyst deposition, and enable rapid release of products. Most

[a] Dr. S. Liu,[+] Y. Zhao,[+] Z. Chen, Dr. D. Gao, F. Feng, Dr. R. Liu, Prof. Dr. C. Streb
Institute of Inorganic Chemistry I
Ulm University
Albert-Einstein-Allee 11, 89081 Ulm, Germany

[b] Y. Zhao,[+] Z. Chen, Dr. D. Gao, F. Feng, T. Rios-Studer, Dr. R. Liu, Prof. Dr. C. Streb
Department of Chemistry
Johannes Gutenberg University Mainz
Duesbergweg 10–14, 55128 Mainz, Germany
E-mail: rongji.liu@uni-mainz.de
carsten.streb@uni-mainz.de

[c] Dr. J. Bansmann
Institute for Surface Chemistry and Catalysis
Ulm University
Albert-Einstein-Allee 47, 89081 Ulm, Germany

[d] J. Biskupek, Prof. Dr. U. Kaiser
Central Facility of Electron Microscopy for Materials Science
Electron Microscopy Group of Material Science
Ulm University
Albert-Einstein-Allee 11, 89081 Ulm, Germany

[+] These authors contributed equally to this work

Supporting information for this article is available on the WWW under https://doi.org/10.1002/celc.202400291

recently, 3D printing has garnered much attention in fabricating electrodes owning to the simple fabricating process, flexible structure building, wide range of printed materials and low cost.[23–26]

This work developed a general method for preparing 3D printed electrodes for the NO_3RR. The commercial thermoplastic polymer acrylonitrile butadiene styrene (ABS) was used, and 3D printed into a microstructured lattice support. Subsequent surface modification of the ABS resulted in the generation of surface carboxyl and amino groups suitable for metal coordination (focus: Ni^{2+}, Cu^{2+}). Then, the NiCu alloy was coated onto the polymer surface by electroless plating. The resulting electrode was tested for the NO_3RR in aqueous media and showed excellent performance. Its integration into an aqueous Zinc-nitrate battery demonstrated the technological utility of the electrode system.

Results and Discussion

The 3D printed electrodes were fabricated in a three-step process involving 3D printing, chemical surface etching, and electroless plating (Scheme 1). The electrodes were designed and 3D printed with a microstructured lattice pattern to increase their surface area and mass transfer properties (Scheme 1 and SI, Figure S1a) based on earlier works by some of us.[27] Based on these reported studies, the ABS polymer surface of the electrode was then oxidized to generate carboxylate and amine binding sites for metal ion coordination (Scheme 1).

To study the impact of the metal composition, we prepared the following electrodes: pure Ni (**Electrode 1**), pure Cu (**Electrode 2**) and bimetallic NiCu alloy (**Electrode 3**). **Electrode 1** was prepared as reported recently by some of us.[27] **Electrode 2** was prepared using a similar method using Cu^{2+} instead of Ni^{2+} for electroless plating (see SI). **Electrode 3** was fabricated by electroless plating with a NiCu alloy. This was achieved using aqueous solutions of $NiSO_4 \cdot 6H_2O$ and $CuSO_4$ which were reduced in a self-catalyzed reaction using NaH_2PO_2 as reductant (see SI). The plating temperature was optimized at 60 °C based on an optimum deposition rate and the low glass transition point of ABS.[27–30] The detailed procedures of preparing three electrodes are described in the SI.

Figure 1a shows the powder X-ray diffraction pattern (pXRD) of **Electrode 1, 2** and **3**. The broad peaks for **Electrode 1** and **Electrode 2** at ~20° are attributed to the printed ABS. This feature was not observed in **Electrode 3** due to the strong NiCu alloy signal. Following Ni electroless plating, new peaks evolve

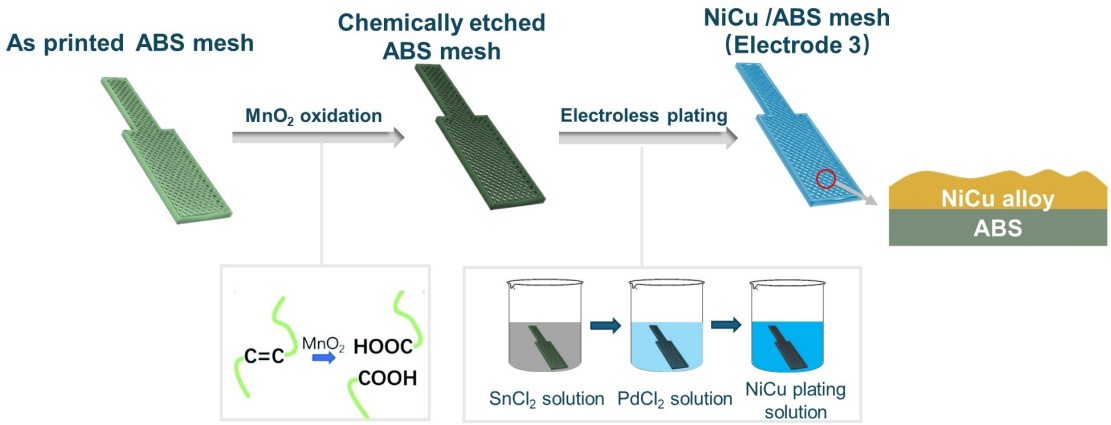

Scheme 1. Schematic illustration of the chemical etching, electroless plating with NiCu metal on 3D printed ABS mesh electrodes.

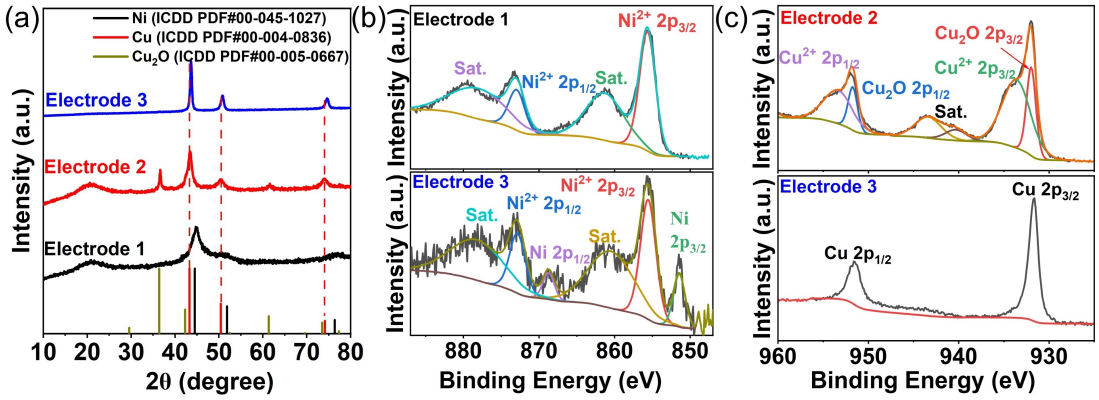

Figure 1. (a) pXRD patterns for **Electrode 1**, **2** and **3**. (b) high resolution XPS spectra of Ni 2p for **Electrode 1** and **3**. (c) high resolution XPS spectra of Cu 2p for **Electrode 2** and **3**.

at ~45°, 52° and 76° correspond to metallic Ni. Similarly, due to the coating of Cu, the pXRD pattern in **Electrode 2** shows prominent metallic Cu peaks at ~43.4°, 50.4°, and 74.0°. It is worth noting that the peaks at ~36.6°and 61.6° demonstrate that part of Cu^{2+} in the plating solution were only be partially reduced to Cu_2O, as previously observed.[31] In **Electrode 3**, there is no discernible signal for Cu_2O, since NaH_2PO_2 was used as strong reducing agent (rather than HCHO used for the synthesis of **Electrodes 1/2)**. The pXRD patterns in Figure 1a illustrate that **Electrode 3** shows signals consistent with a face-centered cubic lattice characteristic for Ni, Cu and their alloys. The larger lattice spacing observed for **Electrode 3** (marked with dashed lines) is due to the increased lattice constants due to the larger atomic radius of Cu compared with Ni.[32,33]

The surface compositions of the electrodes were investigated by X-ray photoelectron spectroscopy (XPS). The survey XPS spectrum of **Electrode 3** shows no Pd was left on the electrode though we used $PdCl_2$ solution during the treatment of ABS substrates (Figure S1d). Figure 1b illustrates that the Ni species on the surface of **Electrode 1** and **Electrode 3** are comparable, showing a main contribution from Ni^{2+},[34] which is presumably formed by surface-oxidation of the metallic nickel deposited. In addition, the signal at 851.4 eV observed for **Electrode 3** indicates the presence of metallic Ni. In contrast, no metallic Ni peak was observed in the **Electrode 1**. This might be resulted from the formation of a thick $NiO/Ni(OH)_2$ surface layers, so that no XPS signal of the underlying Ni metal is observed. The Cu 2p XPS for **Electrode 2** shows the characteristic peaks for Cu(I) (peaks at 951.8 and 932 eV correspond to the Cu(I) $2p_{1/2}$ and Cu(I) $2p_{3/2}$, respectively) and Cu(II) (peaks at 953.6 and 933.8 eV correspond to the Cu(II) $2p_{1/2}$ and Cu(II) $2p_{3/2}$, respectively) species, and the satellite peaks from high-spin Cu(II) ions, indicating the co-existence of Cu_2O and $CuO/Cu(OH)_2$ on the surface (Figure 1c).[35] In comparison, mainly metallic Cu peaks (peaks at 951.6 and 931.7 eV correspond to the Cu(0) $2p_{1/2}$ and Cu(0) $2p_{3/2}$, respectively) are observed for **Electrode 3**, which is consistent with the pXRD result.

The morphology of **Electrode 1** was analyzed by scanning electron microscopy (SEM), which indicates the deposited Ni layer on printed ABS substrate has a wrinkled structure composed of aggregated particles with diameters between ~700 nm to 1.5 μm (SI, Figure S2). In comparison to **Electrode 1**, the electroless Cu coating layer on **Electrode 2** is composed of aggregated particles with a diameter of approximately 500 nm (SI, Figure S3). According to Figure S4a, b, the Cu particles are a mixture of polycrystalline and amorphous structures, which was further confirmed by the selected area electron diffraction (SAED) pattern (SI, Figure S4c). The high-angle annular dark-field scanning-transmission electron microscopy (HAADF-STEM) and corresponding energy-dispersive X-ray spectroscopy (EDX, SI, Figure S5) mapping illustrates the distribution of the main elements, Cu and O, in the coating layers of **Electrode 2**. It is worth noting that there are also C and N with the atomic ratio of C/N = 4/1, confirming the presence of residual EDTA (from the synthesis) on the copper surface.[36] The SEM image of **Electrode 3** shows the NiCu coating layer on printed ABS substrate has a rough surface (Figure S1b,c) contains dense aggregates of nanoparticles with diameters around 100 nm (Figure 2a). While the TEM image of the NiCu coating layer of **Electrode 3** (Figure 2b) demonstrates that the formed NiCu layer has a thick dense stacked structure. The SAED pattern (Figure 2c) shows the randomly ring features which confirm the polycrystalline structure of the plated metal particles. The EDX mapping images of the NiCu coating layer on printed ABS substrate indicate the homogenous distribution of Ni, Cu, O, and P (Figure 2d–g).

To investigate the electrocatalytic NO_3RR performance of the as-prepared electrodes, a three-electrode system with the as-prepared electrodes as working electrode, Pt wire as counter electrode, saturated calomel electrode (SCE) as reference

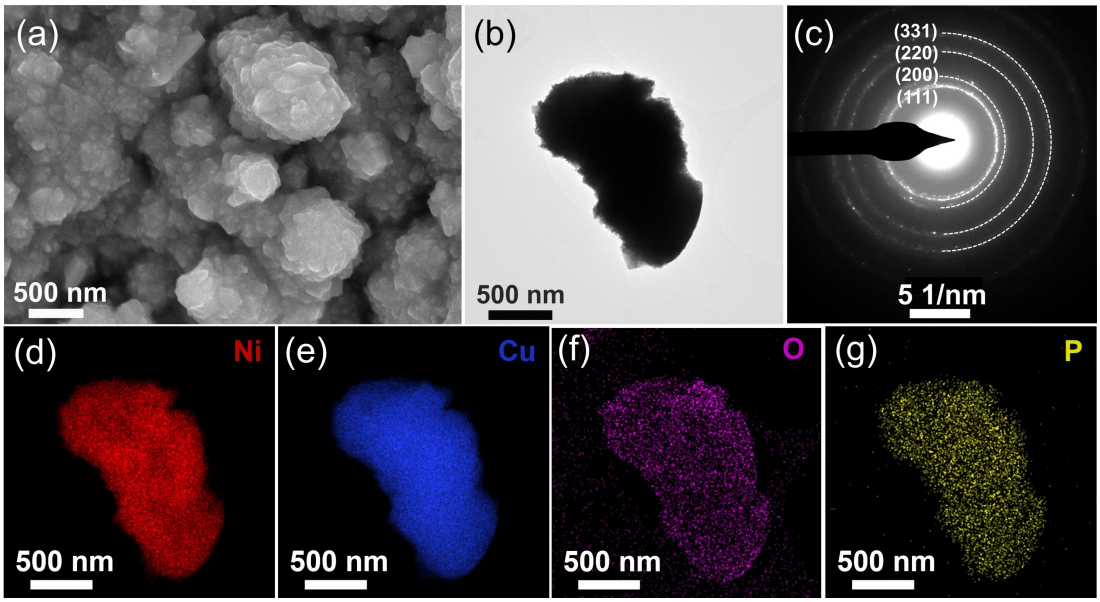

Figure 2. Microscopic characterization of **Electrode 3**. (a) SEM image, (b) TEM image, (c) SAED pattern **3**, (d-g) EDX elemental mapping analysis.

electrode was set up in a H-cell. The anolyte and catholyte were separated by Nafion membrane. To evaluate the performance of the electrodes, linear sweep voltammetry (LSV) curves were collected from 0.4 to −0.8 V vs. RHE in 0.5 M Na_2SO_4 as electrolyte with and without 50 mM $NaNO_3$. In comparison, **Electrode 1** (Figure S6) was more active for the hydrogen evolution reaction (HER) compared with NO_3RR due to the Ni coating,[17] while both the LSV curves of **Electrode 2** (Figure S7) and **Electrode 3** (Figure 3a) show the obvious increase of current density in the presence of NO_3^- with the onset potential at around −0.21 V, indicating the efficient role of Cu based catalysts (here Cu, Cu_2O and $CuO/Cu(OH)_2$) for NO_3RR. Meanwhile, for both **Electrode 2** and **Electrode 3**, the current density increased sharply to its transport-limited value (from −0.4 V to −0.6 V) of ~50 mA/cm^2 for NO_3^- reduction, and then further increased as a result of the occurrence of HER (Figure 3a and SI, Figure S7). The selectivity of **Electrode 1**, **Electrode 2** and **Electrode 3** under various applied potentials was further investigated by 2 h of chronoamperometry in 0.5 M aqueous Na_2SO_4 containing 50 mM $NaNO_3$ (SI, Figures S8–S10). The presence of NH_4^+ and NO_2^- was quantified by UV-vis spectroscopic analyses. To create the calibration curves, a series of electrolytes with known concentrations of NH_4Cl and $NaNO_2$ were measured using a colorimetric approach (SI, Figure S11). Figure 3b and SI, Figure S12 show the corresponding FE of NH_4^+ for **Electrode 1**, **2** and **3**. As shown in Figure 3b, **Electrode 3** shows increasing FE for NH_4^+ within the potential range from −0.18 to −0.38 V, reaching a maximum value of 83% at −0.38 V. However, at −0.48 V and −0.58 V, the FE was slightly reduced to 82% and 70% respectively, which might be related to the competitive undesired HER. In contrast, for **Electrode 1**, the maximum FE was obtained at −0.18 V (62%), then declined linearly to 16% at −0.58 V, indicating the increasing HER selectivity (Figure S12a) when the overpotential is increasing; while for **Electrode 2**, the FE of NH_4^+ indicates a volcano-like distribution with the peak value of 76% at −0.48 V (Figure S12b). The comparison reveals that **Electrode 3** containing Ni and Cu exhibits higher NH_4^+ efficiency than **Electrode 2** containing only Cu in all the investigated potential ranges. The above findings indicate that **Electrode 3** is the most efficient electrode for NO_3^- to NH_3 conversion, possibly owing to the synergistic effect between Ni and Cu.[37] The NH_4^+ yield rate was further calculated to evaluate the performance of **Electrode 3** (Figure 3c). As expected, at the onset potential region of the reaction, **Electrode 3** demonstrates low NH_4^+ yield rate (111 μg/(h cm^2) at −0.18 V) and then it increases to 861 μg/(h cm^2) at −0.38 V. However, this value remains constant even at more negative applied potentials, which is in accordance with the mass-transfer limiting platform (from −0.4 V to −0.6 V) in the LSV curves.[17] It should be noted that **Electrode 1** and **Electrode 2** showed higher NH_4^+ yield rate at some potentials compared with **Electrode 3** (Figure S12c), which may be due to the higher current densities of these electrodes. The NiCu based **Electrode 3** also shows comparable activities with the current reported NiCu based catalysts (Table S1), however this work shows a feasible green method for the synthesis of the electrodes based on the 3D printed substrates.

Further, the effect of NO_3^- concentration on the catalytic performance of **Electrode 3** was also studied. As shown in SI, Figure S13a, the current density in the LSV curves improves as

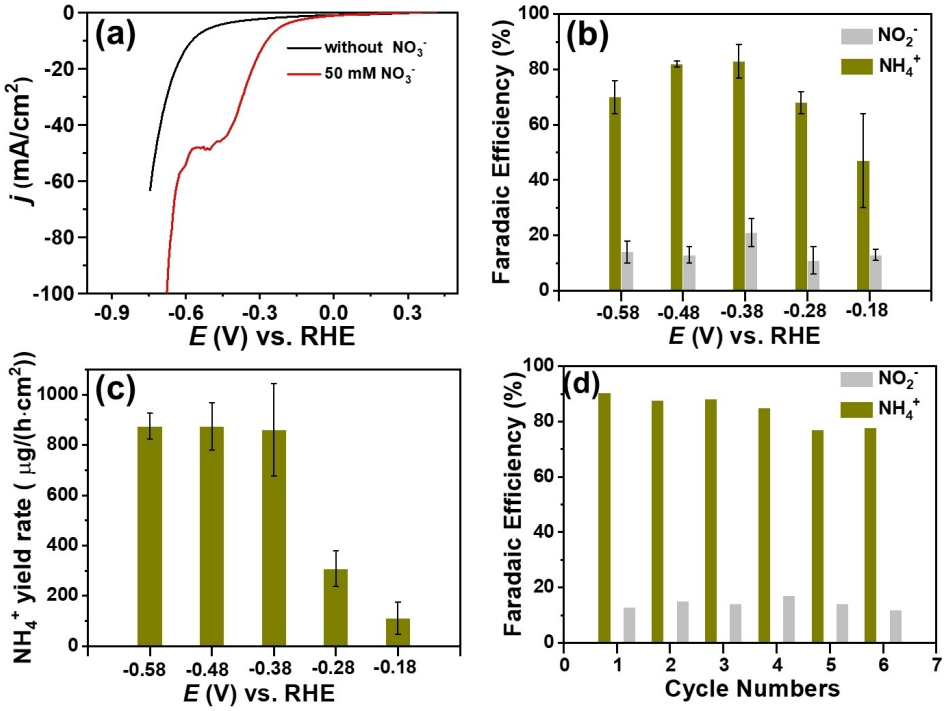

Figure 3. Electrocatalytic NO_3^--to-NH_3 conversion by **Electrode 3**. (a) LSV curves of **Electrode 3** in 0.5 M Na_2SO_4 and 0.5 M Na_2SO_4 + 50 mM $NaNO_3$. (b) FE of NH_4^+ and NO_2^- on the **Electrode 3** at different potentials. (c) NH_4^+ yield rate of **Electrode 3** in 0.5 M Na_2SO_4 + 50 mM $NaNO_3$ at different potentials and (d) Stability test of **Electrode 3** at −0.38 V vs. RHE.

the concentration of $NaNO_3$ increases. Further analyses show that both the FE and yield rate for NH_4^+ were decreased when we increased the concentration of $NaNO_3$ to 100 and 200 mM compared with that in 50 mM, which could be due to the higher NO_2^- selectivity in high nitrate concentration (Figure S13b,c).

The experimental results show that **Electrode 1** (containing Ni) works efficiently as a HER catalyst, while **Electrode 2** (containing Cu) works efficiently for NO_3^- conversion to NH_3. The synergistic effect of Ni and Cu in **Electrode 3** further promotes the NO_3^- to NH_3 conversion, thus increasing the NH_3 selectivity.

It is understood that the conversion of NO_3^- to NH_3 can be separated into a number of elementary reactions. Initially, NO_3^- is adsorbed to form $*NO_3^-$, followed by a series of deoxidation processes ($*NO_3^- \rightarrow *NO_2^- \rightarrow *NO \rightarrow *N$), and subsequently, sequential hydrogenation of *N occurs ($*N \rightarrow *NH \rightarrow *NH_2 \rightarrow *NH_3$).[33,38] It has been reported that Ni alloying with Cu can induce an upshift of the Cu d-band center towards the Fermi level in CuNi alloys, thereby increasing the binding strength of NO_3RR intermediates on the catalyst surface. This enhanced binding suppresses the desorption of intermediates and promotes their further hydrogenation, ultimately leading to increased ammonia production.[17,37]

NMR was used to confirm NH_4^+ amount in the electrolyte and exclude the possible contamination effect from the environment. Similar to the UV-vis approach, the calibration curves were obtained by preparation of reference electrolytes containing known concentrations of $^{14}NH_4Cl$ and $^{15}NH_4Cl$. The intensity of the NMR signals increases as the concentration of $^{14}NH_4Cl$ or $^{15}NH_4Cl$ increases, as shown in SI, Figure S14 a,b, and the ^1H NMR spectra exhibit the characteristic feature of three peaks for $^{14}NH_4Cl$ and two peaks for $^{15}NH_4Cl$. The electrolytes were collected after 2 h electrocatalysis at −0.38 V vs. RHE in the electrolyte containing 50 mM $Na^{14}NO_3$ or $Na^{15}NO_3$. In the $Na^{15}NO_3$ labeled electrolytes, only two peaks emerge in ^1H NMR spectra as shown in SI, Figure S15, indicating that the NH_3 generated is from electrochemical nitrate reduction rather than contamination. The FE for $^{14}NH_4^+$ and $^{15}NH_4^+$ are 73% and 67% respectively.

Long-term stability is another critical criterion in determining the suitability of the electrode for practical application. **Electrode 3** was therefore operated at the optimum conditions (−0.38 V vs. RHE for 2 h in the electrolyte containing 50 mM $NaNO_3$) and recovered, washed, and reused for 6 runs, see SI, Figures S16, S17. The FE of NH_4^+ declined slightly during cycling but remained at 78% in the 6th cycle, indicating of the high stability of **Electrode 3** (Figure 3d). Furthermore, the corresponding FE of NO_2^- underwent little variations during cycling. SEM measurement was used to reveal the potential morphology change for the cycling tested electrode, which shows virtually no changes compared with the fresh samples (SI, Figure S18). In addition, pXRD analysis shows the same characteristic signals as the pre-catalytic sample (SI, Figure S19).

For practical application, we further constructed a novel Zn-nitrate battery utilizing **Electrode 3** as the cathode and zinc foil as the anode (illustrated schematically in Figure 4a).[14,39,40] As depicted in Figure 4b, the battery maintains a constant open

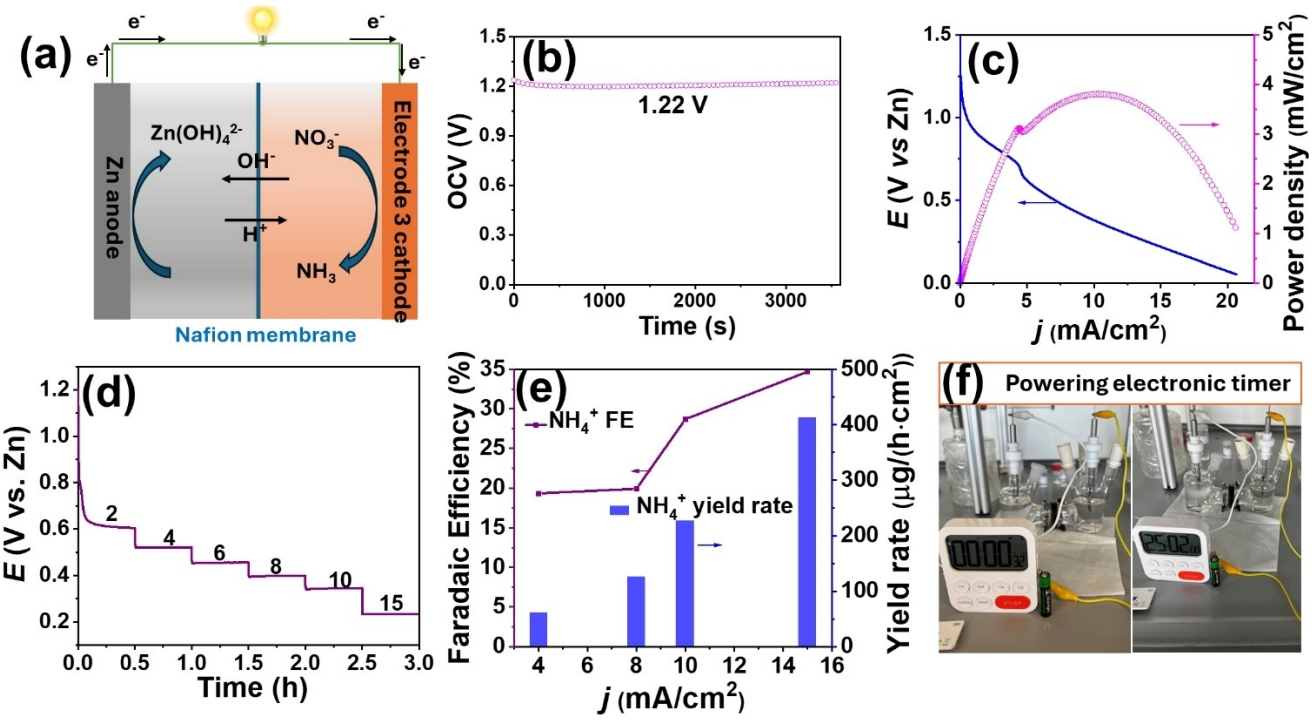

Figure 4. Electrochemical performance of hybrid aqueous Zn-nitrate batteries based on **Electrode 3**. (a) Schematic illustration of the Zn-nitrate battery with Zn anode and **Electrode 3** cathode. (b) Open-circuit voltage of Zn-nitrate battery. (c) Discharge polarization curves and corresponding power density curves of the Zn-nitrate battery. (d) Discharging curves at different current densities of 2, 4, 6, 8, 10 and 15 mA/cm^2. (e) NH_4^+ FE and NH_4^+ yield rate of Zn-nitrate battery after 0.5 h discharging. (f) A photograph of an electronic timer powered by our **Electrode 3** based Zn-nitrate battery, operating for ~25 h.

circuit voltage (OCV) of 1.22 V for at least 1 hour. Figure 4c displays the charge-discharge LSV curves of the **Electrode 3**-based Zn-nitrate battery. The discharge curve demonstrates an increasing output current density as the cathodic potential becomes more negative. The power density of the battery peaks at 3.8 mW/cm^2 (Figure 4c). Figure 4d depicts the time-dependent discharge curves of the Zn-nitrate battery under different currents ranging from 2 to 15 mA/cm^2, indicating good long-term electrochemical stability. Figure 4e illustrates the NH_4^+ yield and corresponding FE during discharge at various output current densities. The **Electrode 3**-based Zn-nitrate battery achieves a high NH_4^+ formation rate of approximately 410 μg/(h cm^2) and attains an FE of 35% at 15 mA/cm^2. Furthermore, the **Electrode 3**-based Zn-nitrate battery powers an electronic timer for at least 25 hours (Figure 4f). In summary, the Zn-nitrate battery system expands the scope of Zn-based batteries. The Zn-nitrate battery system achieves three objectives: sustainable energy supply, NH_3 electrosynthesis and degradation of the NO_3^- pollutant in wastewater.

Conclusions

In summary, we report the design of a 3D printed, Ni–Cu alloy functionalized electrode for efficient nitrate-to-ammonia reduction. When compared with the pure Ni and Cu coated electrodes, the mixed NiCu coated electrode exhibited higher Faradaic efficiency for electrosynthesis of NH_3 from nitrate. In addition, we report high stability and reusability of the electrode. Integration of the electrode into a Zn-nitrate demonstrated its operational capacity for combined sustainable electricity production, NH_3 electrosynthesis, and NO_3^- pollutant degradation. The reported approach could in future allow the facile, scalable design of (multi)functional 3D printed electrode materials.

Acknowledgements

The authors gratefully acknowledge financial support by the Deutsche Forschungsgemeinschaft DFG (TRR 234 CataLight, project number: 364549901 and SPP2370 ''Nitroconversion,'' project no. 501934135) and the German Federal Ministry for Education and Research (BMBF) through the Clusters4Future Initiative (cluster ETOS, project ELFION, project no 03ZU1205EA). R.L. gratefully acknowledges financial support by the Alexander von Humboldt Foundation. D.G. acknowledges the Deutsche Forschungsgemeinschaft (DFG) for a Walter Benjamin Fellowship (project no. 510966757). R.L., D.G., and C.S. gratefully acknowledge financial support by Johannes Gutenberg University Mainz, the Top-Level Research Initiative SusInnoScience and the Gutenberg Research College. Open Access funding enabled and organized by Projekt DEAL.

Conflict of Interests

The authors declare no conflict of interest.

Data Availability Statement

The data that support the findings of this study are available from the corresponding author upon reasonable request.

Keywords: 3D Printing · Electroless Plating · Electrocatalysis · Ammonia synthesis · Zn–Nitrate Batteries

[1] J. W. Erisman, M. A. Sutton, J. Galloway, Z. Klimont, W. Winiwarter, *Nat. Geosci.* **2008**, *1*, 636–639.
[2] G. Ertl, *Angew. Chem. Int. Ed.* **2008**, *47*, 3524–3535.
[3] H. Xu, Y. Ma, J. Chen, W. X. Zhang, J. Yang, *Chem. Soc. Rev.* **2022**, *51*, 2710–2758.
[4] G. Soloveichik, *Nat. Catal.* **2019**, *2*, 377–380.
[5] B. H. R. Suryanto, H.-L. Du, D. Wang, J. Chen, A. N. Simonov, D. R. MacFarlane, *Nat. Catal.* **2019**, *2*, 290–296.
[6] Z. Y. Wu, M. Karamad, X. Yong, Q. Huang, D. A. Cullen, P. Zhu, C. Xia, Q. Xiao, M. Shakouri, F. Y. Chen, J. Y. (Timothy) Kim, Y. Xia, K. Heck, Y. Hu, M. S. Wong, Q. Li, I. Gates, S. Siahrostami, H. Wang, *Nat. Commun.* **2021**, *12*, 1–10.
[7] C. J. M. van der Ham, M. T. M. Koper, D. G. H. Hetterscheid, *Chem. Soc. Rev.* **2014**, *43*, 5183–5191.
[8] H. Wan, A. Bagger, J. Rossmeisl, *Angew. Chem. Int. Ed.* **2021**, *60*, 21966–21972.
[9] T. Hu, C. Wang, M. Wang, C. M. Li, C. Guo, *ACS Catal.* **2021**, *11*, 14417–14427.
[10] Y. Wang, W. Zhou, R. Jia, Y. Yu, B. Zhang, *Angew. Chem. Int. Ed.* **2020**, *59*, 5350–5354.
[11] J. Liang, B. Deng, Q. Liu, G. Wen, Q. Liu, T. Li, Y. Luo, A. A. Alshehri, K. A. Alzahrani, D. Ma, X. Sun, *Green Chem.* **2021**, *23*, 5487–5493.
[12] W. Fu, Z. Hu, Y. Zheng, P. Su, Q. Zhang, Y. Jiao, M. Zhou, *Chem. Eng. J.* **2021**, 133680.
[13] Y. Bu, C. Wang, W. Zhang, X. Yang, J. Ding, G. Gao, *Angew. Chem. Int. Ed.* **2023**, *62*, e202217337.
[14] H. Jiang, G. F. Chen, O. Savateev, J. Xue, L. X. Ding, Z. Liang, M. Antonietti, H. Wang, *Angew. Chem. Int. Ed.* **2023**, *62*, e202218717.
[15] W. Qiu, S. Qin, Y. Li, N. Cao, W. Cui, Z. Zhang, Z. Zhuang, D. Wang, Y. Zhang, *Angew. Chem. Int. Ed.* **2024**, e202402684.
[16] L. Mattarozzi, S. Cattarin, N. Comisso, A. Gambirasi, P. Guerriero, M. Musiani, L. Vázquez-Gómez, E. Verlato, *Electrochim. Acta* **2014**, *140*, 337–344.
[17] Y. Wang, A. Xu, Z. Wang, L. Huang, J. Li, F. Li, J. Wicks, M. Luo, D. H. Nam, C. S. Tan, Y. Ding, J. Wu, Y. Lum, C. T. Dinh, D. Sinton, G. Zheng, E. H. Sargent, *J. Am. Chem. Soc.* **2020**, *142*, 5702–5708.
[18] L. Mattarozzi, S. Cattarin, N. Comisso, R. Gerbasi, P. Guerriero, M. Musiani, E. Verlato, *Electrochim. Acta* **2017**, *230*, 365–372.
[19] D. Reyter, D. Bélanger, L. Roué, *Electrochim. Acta* **2008**, *53*, 5977–5984.
[20] H. Liu, X. Lang, C. Zhu, J. Timoshenko, M. Rüscher, L. Bai, N. Guijarro, H. Yin, Y. Peng, J. Li, Z. Liu, W. Wang, B. R. Cuenya, J. Luo, *Angew. Chem. Int. Ed.* **2022**, *61*, e202202556.
[21] Q. Hu, K. Yang, O. Peng, M. Li, L. Ma, S. Huang, Y. Du, Z. X. Xu, Q. Wang, Z. Chen, M. Yang, K. P. Loh, *J. Am. Chem. Soc.* **2024**, *146*, 668–676.
[22] F. Y. Chen, Z. Y. Wu, S. Gupta, D. J. Rivera, S. V. Lambeets, S. Pecaut, J. Y. T. Kim, P. Zhu, Y. Z. Finfrock, D. M. Meira, G. King, G. Gao, W. Xu, D. A. Cullen, H. Zhou, Y. Han, D. E. Perea, C. L. Muhich, H. Wang, *Nat. Nanotechnol.* **2022**, *17*, 759–767.
[23] J. Lölsberg, O. Starck, S. Stiefel, J. Hereijgers, T. Breugelmans, M. Wessling, *ChemElectroChem* **2017**, *4*, 3309–3313.
[24] V. A. Beck, A. N. Ivanovskaya, S. Chandrasekaran, J. B. Forien, S. E. Baker, E. B. Duoss, M. A. Worsley, *Proc. Natl. Acad. Sci. USA* **2021**, *118*, e2025562118.
[25] Z. Lyu, G. J. H. Lim, J. J. Koh, Y. Li, Y. Ma, J. Ding, J. Wang, Z. Hu, J. Wang, W. Chen, Y. Chen, *Joule* **2021**, *5*, 89–114.
[26] W. Zhang, H. Liu, X. Zhang, X. Li, G. Zhang, P. Cao, *Adv. Funct. Mater.* **2021**, 2104909.

[27] S. Liu, R. Liu, D. Gao, I. Trentin, C. Streb, *Chem. Commun.* **2020**, *56*, 8476–8479.
[28] H. S. Yu, S. F. Luo, Y. R. Wang, *Surf. Coat. Technol.* **2001**, *148*, 143–148.
[29] F. Yang, B. Yang, B. Lu, L. Huang, S. Xu, S. Zhou, *Acta Phys.-Chim. Sin.* **2006**, *22*, 1317–1321.
[30] J. Georgieva, S. Armyanov, *J. Solid State Electrochem.* **2007**, *11*, 869–876.
[31] J. Eskhult, M. Herranen, L. Nyholm, *J. Electroanal. Chem.* **2006**, *594*, 35–49.
[32] J. Zhang, M. D. Baró, E. Pellicer, J. Sort, *Nanoscale* **2014**, *6*, 12490–12499.
[33] L. Fang, S. Wang, C. Song, X. Yang, Y. Li, H. Liu, *J. Hazard. Mater.* **2022**, *421*, 126628 (1–9).
[34] M. C. Biesinger, B. P. Payne, A. P. Grosvenor, L. W. M. Lau, A. R. Gerson, R. S. C. Smart, *Appl. Surf. Sci.* **2011**, *257*, 2717–2730.
[35] M. C. Biesinger, L. W. M. Lau, A. R. Gerson, R. S. C. Smart, *Appl. Surf. Sci.* **2010**, *257*, 887–898.
[36] J. Liu, J. Fu, Y. Zhou, W. Zhu, L. P. Jiang, Y. Lin, *Nano Lett.* **2020**, *20*, 4823–4828.
[37] Y. Liu, B. Deng, K. Li, H. Wang, Y. Sun, F. Dong, *J. Colloid Interface Sci.* **2022**, *614*, 405–414.
[38] S. Han, H. Li, T. Li, F. Chen, R. Yang, Y. Yu, B. Zhang, *Nat. Catal.* **2023**, *6*, 402–414.
[39] Y. Guo, R. Zhang, S. Zhang, Y. Zhao, Q. Yang, Z. Huang, B. Dong, C. Zhi, *Energy Environ. Sci.* **2021**, *14*, 3938–3944.
[40] Y. Liu, R. Cheng, H. Ren, T. Sun, D. Liu, *ACS Sustainable Chem. Eng.* **2024**, *12*, 3780–3789.

Manuscript received: April 4, 2024
Revised manuscript received: June 3, 2024
Version of record online: July 15, 2024